



Title	Two types of amorphous protein particles facilitate crystal nucleation
Author(s)	Yamazaki, Tomoya; Kimura, Yuki; Vekilov, Peter G.; Furukawa, Erika; Shirai, Manabu; Matsumoto, Hiroaki; Van Driessche, Alexander E. S.; Tsukamoto, Katsuo
Citation	Proceedings of the National Academy of Sciences of the United States of America (PNAS), 114(9), 2154-2159 <a href="https://doi.org/10.1073/pnas.1606948114">https://doi.org/10.1073/pnas.1606948114</a>
Issue Date	2017-01-10
Doc URL	<a href="http://hdl.handle.net/2115/66517">http://hdl.handle.net/2115/66517</a>
Type	article (author version)
File Information	Main_PNAS_accepted -.pdf



[Instructions for use](#)

1 **Two types of amorphous protein particles facilitate crystal nucleation**

2 **(Short title): Two-type protein particles ease crystallization**

3  
4 Tomoya Yamazaki<sup>1,2</sup>, Yuki Kimura<sup>1\*</sup>, Peter G. Vekilov<sup>3</sup>, Erika Furukawa<sup>2</sup>, Manabu  
5 Shirai<sup>4</sup>, Hiroaki Matsumoto<sup>4</sup>, Alexander E. S. Van Driessche<sup>5</sup>, Katsuo Tsukamoto<sup>2</sup>

6  
7 <sup>1</sup>Institute of Low Temperature Science, Hokkaido University, Kita-19, Nishi-8, Kita-ku,  
8 Sapporo, 060-0819, Japan.

9 <sup>2</sup>Department of Earth Science, Graduate School of Science, Tohoku University, 6-3,  
10 Aramaki Aza Aoba, Aoba-ku, Sendai, Miyagi 980-8578, Japan.

11 <sup>3</sup>Department of Chemical and Biomolecular Engineering and Department of Chemistry,  
12 University of Houston, 4726 Calhoun Boulevard, Houston, Texas 77204-4004, USA.

13 <sup>4</sup>Hitachi High-Technologies Corporation, 11-1, Ishikawa-cho, Hitachinaka-shi, Ibaraki  
14 312-0057, Japan.

15 <sup>5</sup>Structural Biology Brussels, Vrije Universiteit Brussel, Pleinlaan 2, 1050 Elsene,  
16 Brussels, Belgium.

17  
18 \*To whom correspondence should be addressed; E-mail:  
19 [ykimura@lowtem.hokudai.ac.jp](mailto:ykimura@lowtem.hokudai.ac.jp) TEL: +81-11-706-7666

20  
21 *Classification*

22 PHYSICAL SCIENCE: Applied Physical Science

23  
24 *Keywords*

25 Nucleation, Protein, Lysozyme, Crystal, Transmission electron microscopy, In-situ  
26 observation

27

28 **Abstract**

29 Nucleation, the primary step in crystallization, dictates the number of crystals, the  
30 distribution of their sizes, the polymorph selection, and other crucial properties of the  
31 crystal population. We employed time-resolved liquid-cell transmission electron  
32 microscopy (TEM) to perform an in situ examination of the nucleation of lysozyme  
33 crystals. Our TEM images revealed that mesoscopic clusters, which are similar to those  
34 previously assumed to consist of a dense liquid and serve as nucleation precursors, are  
35 actually amorphous solid particles (ASPs) and act only as heterogeneous nucleation  
36 sites. Crystalline phases never form inside them. We demonstrate that a crystal appears  
37 within a non-crystalline particle assembling lysozyme on an ASP or a container wall,  
38 highlighting the role of heterogeneous nucleation. These findings represent a significant  
39 departure from the existing formulation of the two-step nucleation mechanism while  
40 reaffirming the role of non-crystalline particles. The novel insights gained may have  
41 significant implications in areas that rely on the production of protein crystals, such as  
42 structural biology, pharmacy, and biophysics, and for the fundamental understanding of  
43 crystallization mechanisms.

44

45

46 **Significance**

47 The formation of the nuclei of protein crystals has been suggested to occur within  
48 protein-rich mesoscopic clusters. The existence of such clusters has been revealed for  
49 many proteins; however, their role in crystallization is still unclear. Our live images in a  
50 protein crystallization solution using transmission electron microscopy reveal that  
51 protein-rich mesoscopic clusters are solid amorphous particles that work as  
52 heterogeneous nucleation sites. The nucleation event for the crystal starts via another  
53 non-crystalline particle, which appears only a few seconds before crystal nucleation, i.e.,  
54 there are two types of amorphous particles that have different roles in protein  
55 crystallization.

56

57 Crystallization can be divided into two processes: nucleation and crystal growth.  
58 The crystal growth process has been well examined for a long time, yet the nucleation  
59 process is not understood; for example, the nucleation rate of crystals provides a  
60 textbook example of order-of-magnitude discrepancies between theoretical predictions  
61 and experimental results. Recent proposals have attributed these discrepancies to a  
62 non-classical nucleation pathway, along which a structured crystalline embryo forms  
63 within a highly concentrated disordered precursor (1). This mechanism was first  
64 proposed for protein crystals (2, 3). Direct observations have demonstrated its  
65 applicability to organic (4), inorganic (5, 6), and colloidal (7) crystals. In proteins,  
66 clusters of protein molecules have been suggested as precursors; these clusters have  
67 mesoscopic sizes from several tens to several hundreds of nanometers and are  
68 considered to behave like liquids. It has also been suggested that the precursor is  
69 thermodynamically stable with respect to the mother liquid phase but is metastable or  
70 unstable with respect to the crystalline phase. The latter nature of the precursor differs  
71 from the stable macroscopically dense liquid formed as a result of the liquid–liquid  
72 phase separation (8). Such protein-rich mesoscopic clusters have been observed for  
73 many proteins, primarily using optical techniques, and have been tentatively identified  
74 as precursors for crystal nucleation (9–12). Several important questions concerning this  
75 mechanism remain unanswered. First, are the observed mesoscopic clusters actually  
76 liquid-like or solid-amorphous? Second, do they play an active role in crystal  
77 nucleation? And finally, do the clusters serve as classical heterogeneous nucleation  
78 centers or as loci of enhanced non-classical nucleation? To address these questions, we  
79 employed time-resolved *in situ* transmission electron microscopy (TEM) with a liquid  
80 cell (Fig. S1) to directly observe crystal nucleation with the protein lysozyme, arguably  
81 the most closely studied enzyme (13).

82

83

## 84 **Results and Discussion**

85

### 86 **Analysis of the crystallization solutions**

87 To accelerate nucleation, the liquid cell was initially charged with an unfiltered  
88 crystallization solution (50 mg mL<sup>-1</sup> of lysozyme and 5 wt% NaCl in a sodium acetate  
89 buffer solution); subsequently, a filtered growth solution (15 mg mL<sup>-1</sup> of lysozyme and  
90 5 wt% NaCl in a sodium acetate buffer solution) was continuously passed through the  
91 liquid cell to maintain a constant concentration. Both solutions were analyzed using  
92 dynamic light scattering (DLS) (Fig. S2). The DLS signal from the unfiltered solutions

93 is nearly identical to numerous published datasets collected under similar conditions  
94 that reveal the presence of mesoscopic (diameters > 100 nm) clusters, which have been  
95 suggested to act as precursors for crystal nucleation (9, 10). These solutions clearly lie  
96 outside the liquid–liquid coexistence region of the phase diagram, indicating that stable  
97 macroscopic dense liquids should not form under these conditions (8). The DLS  
98 characterization of the filtered solutions reveals the presence of only lysozyme  
99 monomers (Fig. S2).

100

### 101 ***In situ* TEM observations**

102 *In situ* TEM observations (Fig. 1A) demonstrate particles with a range of sizes similar  
103 to those identified using DLS. Most of the particles were immobile because they were  
104 attached to the liquid cell windows. The mean diameter of the particles was estimated  
105 directly from the TEM images to be ~170 nm (Fig. S3A). The electron-diffraction  
106 patterns of the particles exhibit halo rings and no diffraction contrast in the bright field  
107 images (Fig. 1D). Furthermore, they did not coalesce even though many of them were in  
108 direct contact with each other. Amorphous particles were also confirmed by  
109 corresponding diffraction patterns from the cryo-TEM observations (Figs. S3B and  
110 S3C). Note that the particles could not be observed in the filtered solutions. From these  
111 observations, we conclude that the particles are amorphous solid particles (ASPs) of  
112 lysozyme. The ASPs are similar in size to the mesoscopic clusters, which have been  
113 suggested to be precursors for crystal nucleation, as reported in previous studies (9, 10).  
114 However, crystals never formed within the ASPs during our observations.

115 In multiple experiments, we observed both orthorhombic and tetragonal crystals in  
116 addition to the ASPs (Fig. 1). The morphologies of the crystals were similar to those of  
117 corresponding macroscopic crystals that form under similar conditions (14, 15). For  
118 additional identification, we analyzed the electron-diffraction patterns generated by  
119 these crystalline phases (Figs. 1E and 1F). The long-term evolution of two crystals  
120 growing in close proximity (Fig. S4) revealed that the orthorhombic crystals grew while  
121 the tetragonal crystals dissolved, indicating that the former are more stable polymorphs  
122 under the tested experimental conditions. In addition, we observed orthorhombic  
123 lysozyme crystals and ASPs in the same view (Fig. S5). The ASPs dissolved completely  
124 as opposed to the stably existing orthorhombic lysozyme crystals, suggesting the lower  
125 solubility of the orthorhombic lysozyme crystal than that of the ASPs, i.e., orthorhombic  
126 crystals are more stable than ASPs under the experimental conditions.

127 During more than 60 h in 30 separate experiments under optimized experimental  
128 conditions, we monitored the nucleation events of an orthorhombic lysozyme crystal

129 attached to a silicon nitride window (Fig. 2A and Movie S1). First, a spherical particle  
130 (indicated by an arrowhead in Fig. 2A) formed. As it grew, the particle attained crystal  
131 facets and, finally, transformed into an orthorhombic crystal with a characteristic shape  
132 elongated in the  $\langle 001 \rangle$  direction. In other experiments, we observed the nucleation of  
133 orthorhombic crystals on ASPs (Fig. 2B and Movie S2). A spherical particle (indicated  
134 by an arrowhead in Fig. 2B) was observed to nucleate and transform into an  
135 orthorhombic crystal. Because the initial particle has a weaker contrast than that of an  
136 ASP at the same size, the nucleated particle may have a different internal structure and  
137 density, or shape, than that of the ASPs. This observation clearly indicates that the  
138 nucleation event did not start within the ASP; instead, the ASP acted as a heterogeneous  
139 substrate that enhanced the nucleation event.

140 To test the role of the ASPs in the nucleation process, we filtered the  
141 crystallization solution. TEM and DLS observations (Fig. S2) indicated that the ASPs  
142 were removed from the filtered solutions. Then, the nucleation rates were drastically  
143 reduced, likely as a result of the lack of heterogeneous substrates (9). Therefore, the  
144 participation of the ASPs as heterogeneous substrates is crucial to crystal nucleation in  
145 this system.

146

### 147 **Evolution of the growth rates of nucleated particles**

148 For additional insight into the nucleation process, we compared the evolution of the  
149 lysozyme particle growth rates with known crystal growth rates. We measured the time  
150 dependence of the size ( $L$ ) of the two nucleated particles defined by the bidirectional  
151 arrows in Figs. 2A and 2B. The size evolutions in Fig. 3 demonstrate that, immediately  
152 after nucleation as the first stage of growth, both particles grew to a size of over 100 nm  
153 within approximately 0.1 s i.e., the growth rate was close to  $1 \mu\text{m s}^{-1}$ ; then, the particles  
154 grew nearly constantly, and the growth rates of this stage were approximately  $1.72 \pm$   
155  $0.22 \text{ nm s}^{-1}$  and  $1.73 \pm 0.23 \text{ nm s}^{-1}$ , as obtained from the datasets of  $L1$  and  $L2$ ,  
156 respectively, in Fig. 3 at 10–30 s. The growth rates at the initial stage are faster by over  
157 two orders of magnitude than those during the steady state, which are the same as  
158 macroscopic lysozyme (or any other protein) crystals at similar supersaturations (15–  
159 17).

160 To analyze the evolution of the growth rate after nucleation, we first evaluated the  
161 effects of the electron beam, which increases the temperature of the specimen (18) and  
162 generates chemical species (19), on our system. We observed the growth of  
163 orthorhombic lysozyme crystals under different electron fluxes (Fig. S6 and Movie S3).  
164 At an electron flux of  $3.2 \times 10^2 \text{ electron nm}^{-2} \text{ s}^{-1}$ , the crystal grows continuously.

165 However, when we increased the electron flux to  $2.9 \times 10^3$  electron  $\text{nm}^{-2} \text{s}^{-1}$ , the crystal  
166 started to dissolve. In addition, we observed that the growth rate at  $3.2 \times 10^2$  electron  
167  $\text{nm}^{-2} \text{s}^{-1}$  is constant, at least for 60 s, at a rate of  $1.68 \pm 0.03$   $\text{nm s}^{-1}$  (Figs. S7A and B).  
168 We also measured the growth rate of orthorhombic lysozyme crystals in a non-electron  
169 irradiated environment using optical microscopy (Fig. 7C). At the same conditions as  
170 the TEM, the growth rate measured by optical microscopy is  $1.7$   $\text{nm s}^{-1}$ , indicating that  
171 the electron beam does not have a significant effect on our system at  $3.2 \times 10^2$  electron  
172  $\text{nm}^{-2} \text{s}^{-1}$ .

173 Between 0.1 s and 10 s, the growth rates of the two particles sharply decreased  
174 from several hundreds of  $\text{nm s}^{-1}$  to the bulk growth rate. This appears to be the same  
175 tendency as in the case of the nucleation of inorganic materials, such as  $\text{AgNO}_3$  (20) and  
176  $\text{CaCO}_3$  (21). Based on the Lifshitz–Slyozov–Wagner theory, which can evaluate  
177 whether the crystal growth is controlled by diffusion or surface kinetics, these growth  
178 rates were limited by diffusion processes because the growth units around the particles  
179 were depleted due to the more rapid incorporation of the growth units into the crystals  
180 compared to the supply of the growth units to the particle surfaces by diffusion.  
181 However, it is well known that the growth of lysozyme crystals is not limited by the  
182 diffusion process. Therefore, we first evaluated the possibility of solution depletion as a  
183 result of particle formation as a process underlying the slowdown of growth. We used  
184 the fact that lysozyme is a relatively small molecule with a hydrodynamic diameter of  
185 approximately 3.2 nm and a diffusivity  $D$  of approximately  $100 \mu\text{m}^2 \text{s}^{-1}$ . The Stokes–  
186 Einstein relation,  $l^2 = D \Delta t$ , reveals that diffusion over the characteristic length  $l = 100$   
187 nm, the particle size, would occur over times,  $\Delta t$ , of an order of 0.1 ms. This estimation  
188 indicates that the solution concentration at the particle growth interface is replenished  
189 within times much shorter than those probed in Fig. 3. Detailed numerical calculations  
190 of the diffusive solute supply (where buoyancy-driven convection is suppressed in cells  
191 with a height of 150 nm or 500 nm, as used here) and the decrease in growth rate  
192 support this conclusion (Supporting Information and Fig. S8). Accordingly, we attribute  
193 the growth slowdown to the evolution of the particle structure.

194 Growth rates faster than those recorded for faceted crystals at similar conditions  
195 (15–17) suggest that molecules encounter lower barriers en route to the particle surface.  
196 There are three barriers to the growth of a new phase: an enthalpy barrier related to the  
197 creation of bonds in the condensed phase, solid or liquid (22), and two entropy barriers,  
198 which account for the search for an incorporation site, via translational diffusion, and a  
199 proper crystallographic orientation, via rotational diffusion (23). Molecular  
200 incorporation into faceted crystals, where the growth sites on the smooth crystal

201 surfaces are few and distant, and relatively strong crystal bonds are created, maximizing  
202 the values of all three barriers. Associations with liquid droplets or clusters encounter  
203 minimal entropic barriers and a reduced activation enthalpy. Incorporation into rough  
204 crystals, in which the growth site density is close to one, is an intermediate case, where  
205 the enthalpy and rotational barriers are close to those of a faceted crystal, whereas the  
206 translational barrier is minimal. Therefore, the initial growth rates (several hundreds of  
207  $\text{nm s}^{-1}$ ) recorded immediately after nucleation suggest the growth of non-crystalline  
208 particles, and the intermediate growth rates (several tens to several  $\text{nm s}^{-1}$ ) recorded  
209 between 1 s and 10 s suggest the growth of rough crystals, as expected for crystals  
210 emerging from non-crystalline particles. This conclusion is supported by the growth rate  
211 of steps on the surface of an orthorhombic lysozyme crystal,  $44 \text{ nm s}^{-1}$  (Fig. S9); the  
212 steps are always rough and offer the same barriers for molecular incorporation as rough  
213 crystals. Therefore, in the case of protein crystallization, entropic restrictions are  
214 important due to the large size and complex shape of these molecules. This is one of the  
215 reasons why the kinetic coefficients of proteins are 10–1000 times lower than those of  
216 inorganic crystals (24). Therefore, it is reasonable to assume that the very large growth  
217 rates measured for the initial particles are only achievable for non-crystalline structures  
218 (i.e. eliminating part of the entropic restrictions).

219 At times longer than 30 s, the growth rate of the two crystals dropped to  $1.24 \pm$   
220  $0.11 \text{ nm s}^{-1}$  and  $1.37 \pm 0.17 \text{ nm s}^{-1}$  (obtained from the each dataset at 30–60 s),  
221 respectively. TEM images reveal that the phases present during this later stage are  
222 faceted crystals. The growth rates measured from the TEM images are similar to those  
223 of bulk crystals (Fig. S7) and suggest that the crystals grew following a layer-growth  
224 mode (14).

225 We use the late stage growth rates to evaluate potential artifacts due to irradiation  
226 by the electron beam. The consistency between growth rates measured by TEM and  
227 those measured by optical microscopy (Fig. S7C) indicate that the electron-beam  
228 irradiation negligibly affects the nucleation and growth processes. Assuming that the  
229 gradual slowdowns of late-stage growth are due to solution heating by the electron  
230 beam, the roughly estimated value of the maximum temperature elevation at the center  
231 of the beam is  $1.33 \text{ }^\circ\text{C}$  under our typical experimental condition (18) (details are  
232 provided in the Supplementary Information). If we use the temperature dependency of  
233 the solubility and the growth rate (Fig. S7C) to evaluate the hypothetical temperature  
234 increase, the growth rate of  $\sim 1.3 \text{ nm s}^{-1}$  at 30–60 s (Fig. 3) suggests a temperature  
235 elevation of  $0.3 \text{ }^\circ\text{C}$ . Typically, to monitor a larger solution volume, we shifted the view  
236 field after approximately 10 s of observation. Therefore, the solution overheating in

237 these scans was less than 0.1 °C and the corresponding decrease in the supersaturation  
238 was insignificant.

239

#### 240 **Nucleation process of lysozyme crystals**

241 To demonstrate the appearance of a crystal within a non-crystalline particle, we show  
242 cryo-TEM images in Fig. 4. The ununiformed contrast can be observed from the particle  
243 shown in Fig. 4A. A Laue spot in the corresponding diffraction pattern (Fig. 4B), the  
244 faceted shape, and the corresponding diffraction contrast (Fig. S10) represent the  
245 crystalline phase. These cryo-TEM images may show that a crystal appears within a  
246 non-crystalline particle. To precisely prove the appearance of a crystal in a  
247 non-crystalline particle, three-dimensional images may be useful because a TEM image  
248 is just a projection. In summary, time-resolved in situ TEM observations of  
249 supersaturated solutions of the protein lysozyme demonstrated crystal nucleation  
250 following a heretofore-unsuspected modification of the two-step mechanism. Based on  
251 the observations, the pathways of this mechanism are schematically illustrated in Fig. 5.  
252 In contrast to earlier proposals (2, 3, 9–12), we demonstrate the action of two  
253 mesoscopic amorphous phases: amorphous solid particles that serve as heterogeneous  
254 nucleation substrates and short-lived (approximately 0.1 s) non-crystalline particles,  
255 which form on the container wall or the ASPs and host crystal nuclei. Even though the  
256 detailed features of the non-crystalline particles are still unclear, a plausible feature is  
257 that of a dense liquid because molecules inside the particles have the flexibility to form  
258 crystalline structures, which may be a feature of the liquid phase. Importantly, lysozyme  
259 molecules do not directly assemble into crystal nuclei and the ASPs never transform  
260 into crystals. This observation gives us insights into the nucleation of not only protein  
261 crystals but also other organic crystals. Scattering and spectroscopic techniques reveal  
262 the structure evolutions of organic materials in solutions and the existence of clusters  
263 (25). To understand the nucleation, our observations suggest the importance of the direct  
264 observation of nucleation events at the nanoscale to reveal the role of amorphous  
265 particles on crystal nucleation, whether they act as heterogeneous nucleation sites or  
266 precursors for nucleation. In addition, numerous organic molecules of sizes larger than 1  
267 nm have become the focus of medicinal and pharmaceutical chemists (26). It is likely  
268 that the large size and related flexibility of these molecules may invoke in their  
269 solutions behaviors similar to those observed with proteins, including the complex  
270 nucleation pathways reported here. Such a complex pathway has also been observed  
271 using cryo-TEM in organic materials, where the amorphous material that is initially  
272 formed is reorganized into an ordered system (27).

273 We demonstrate that the crystals emerging from the non-crystalline particles are  
274 rough and follow a normal growth mode, with faceting attained at later growth stages.  
275 For additional insights, further analyses of observed non-crystalline particles, such as  
276 formation kinetics, are required.

277

278

## 279 **Materials and Methods**

280

### 281 **Materials**

282 Six-times-recrystallized lysozyme powder (Lot No. E40314; Seikagaku Kogyo Co. Ltd.,  
283 Tokyo) was used as a protein sample without further purification. A 50 mM solution of  
284 sodium acetate (pH = 4.5) was used as the buffer solution. Stock solutions of lysozyme  
285 were prepared by dissolving the appropriate amount of lysozyme powder in the buffer  
286 solution. The concentration of the lysozyme stock solutions was measured using UV  
287 absorption spectrometry (SmartSpec Plus; Bio-Rad Laboratories, Inc., Berkeley, CA).  
288 NaCl (99.99%; Wako Pure Chemical Industries, Ltd., Osaka) was dissolved in the buffer  
289 solution to act as a precipitant for the lysozyme. The crystallization solution was  
290 prepared by mixing appropriate amounts of the stock solutions. The lysozyme powder  
291 sample contained ~1.5% impurities, which consisted primarily of lysozyme dimer and  
292 18-kDa polypeptide (28).

293

### 294 **Solution preparation and procedure for time-resolved liquid-cell TEM** 295 **observations**

296 The supersaturation of the crystallization solution is defined as  $\sigma = \ln(C/C_e)$ , where  $C$  is  
297 the bulk concentration of lysozyme and  $C_e$  is its solubility at a given temperature. We  
298 used two crystallization solutions with different supersaturations. A crystallization  
299 solution with a higher supersaturation was used to initially fill the liquid cell before the  
300 observation. This solution was prepared by mixing the lysozyme solution and NaCl  
301 solution immediately before filling the liquid cell. The resulting solution contained 50  
302 mg mL<sup>-1</sup> lysozyme and 50 mg mL<sup>-1</sup> NaCl and was not filtered. The crystallization  
303 solution, with a lower supersaturation, contained 15 mg mL<sup>-1</sup> lysozyme and 50 mg  
304 mL<sup>-1</sup> NaCl, and flowed through the liquid cell during the TEM observations. This  
305 crystallization solution was filtered through a cellulose acetate filter with 0.20- $\mu$ m pores.  
306 During the observations, the solution was passed continuously through the liquid cell at  
307 a rate of 1–3  $\mu$ L min<sup>-1</sup> by means of a syringe pump. All our experiments were  
308 performed at 24 °C; as a result, the degree of supersaturation,  $\sigma$ , in the liquid cell was

309 constant. We used values of  $3.19 \text{ mg mL}^{-1}$  and  $3.30 \text{ mg mL}^{-1}$  as the solubilities at  $24 \text{ }^\circ\text{C}$   
310 for the orthorhombic (29) and tetragonal phases (30), respectively, to maintain  
311 consistency with our observations of the stability of these phases (Fig. S4). The  
312 supersaturations of the crystallization solution with the lower supersaturation were  $\sigma =$   
313  $1.55$  and  $\sigma = 1.51$  for the orthorhombic and tetragonal forms, respectively.

314

### 315 **Electron microscopy**

316 We used two Hitachi transmission electron microscopes: a H-8100 and a HF-3300. The  
317 H-8100 with a  $\text{LaB}_6$  filament was operated at an acceleration voltage of 200 kV. Images  
318 and movies were recorded using an XR-611 TEM camera (Advanced Microscopy  
319 Techniques, Woburn, MA), which has a recording interval of 157 ms. The HF-3300  
320 with a field-emission gun was operated at an acceleration voltage of 300 kV. Movies  
321 were recorded using an ORIUS SC1000 CCD TEM camera (Gatan Inc. Pleasanton, CA,  
322 USA), which had a recording interval of 100 ms. The electron flux was measured using  
323 a combination of a probe-current detector and a Model 6485 Picoammeter (Keithley  
324 Instruments Inc. Solon, OH, USA) installed in the H-8100.

325

### 326 **The TEM holder and the assembly of the liquid cell**

327 We used a TEM holder (Protochips, Inc., Raleigh, NC) in combination with a liquid cell  
328 to image the liquids. The liquid cell consisted of a pair of semiconductor-based plates  
329 with an electron-transparent window consisting of an amorphous silicon nitride  
330 membrane and two Viton O-rings. These components permitted the preparation of the  
331 sample solution under high-vacuum conditions in the TEM (Fig. S1) and allowed the  
332 solution to be passed through the liquid cell by means of a syringe pump during the  
333 observations. The plates were separated by 150-nm-thick or 500-nm-thick spacers to  
334 form the flow path for the sample solution. The thickness of the observed solution layer  
335 was larger than the thickness of the spacer due to the expansion resulting from the  
336 vacuum present in the electron microscope (31). Before assembling the liquid cell, the  
337 plates were subjected to a hydrophilization treatment using plasma-ion bombardment.

338

### 339 **Rates of growth of the lysozyme crystals examined using optical microscopy**

340 We observed orthorhombic lysozyme crystals using phase-contrast microscopy (PCM),  
341 and we measured their growth rates for comparison with those observed using TEM.  
342 For these measurements, we used a growth cell (32) in which a seed crystal and the  
343 growth solution were sealed. Seed crystals for the PCM observations were produced  
344 using a crystallization solution ( $100\text{--}120 \text{ mg mL}^{-1}$  lysozyme +  $25 \text{ mg mL}^{-1}$  NaCl in the

345 buffer solution). The solution was sealed in a glass tube (~400 mL) and kept in an  
346 incubator at 40 °C to produce orthorhombic crystals. After 2–3 days, several crystals  
347 measuring 100–200 μm were formed, and these were used as seed crystals. A seed  
348 crystal was placed in the cell and aligned with its *c*-axis parallel to the focal plane. The  
349 growth solution, which contained 15 mg mL<sup>-1</sup> lysozyme and 50 mg mL<sup>-1</sup> NaCl, was  
350 identical to that used in the experiments in the TEM. Before the growth solution was  
351 sealed in the cell, it was filtered using a syringe filter with a pore size of 0.20 μm. For  
352 the growth-rate measurements, the temperature of the cell was maintained in the range  
353 of 24–28 °C using Peltier elements on the cell stage. The range of supersaturation  $\sigma$  of  
354 the solutions was 1.38–1.55 for the orthorhombic crystals. The temperature at which we  
355 measured the step velocity for the orthorhombic crystal (Fig. S7) was 24 °C; the  
356 corresponding supersaturation  $\sigma$  was 1.55.

357

### 358 **Dynamic light scattering characterization of the solutions**

359 The correlation functions of light scattered by the tested solutions were recorded using  
360 an ELS-Z1TK instrument (Otsuka Electronics Co., Ltd., Japan, Osaka) equipped with a  
361 semiconductor laser (wavelength: 660 nm). We used a quartz cuvette. The respective  
362 correlation functions of these solutions are shown in Fig. S2.

363

### 364 **Cryo-TEM observations**

365 We used a field emission TEM, JEM-2200FS, operated at an acceleration voltage of 200  
366 kV. Images were corrected using a MSC Model 794 (Gatan Inc. Pleasanton, CA, USA).  
367 The sample solution was put on a micro grid, moved to a cryo-treatment, and was  
368 placed on the cryo-TEM holder. After the treatment, the grid was maintained  
369 continuously under -170 °C to prevent crystallization of the water.

370

### 371 **Determination of the size of the ASPs**

372 From the TEM images, we measured the mean diameter of the ASPs in the experimental  
373 solution. An example image is shown in Fig. S3. The ASPs were counted and the  
374 surface area occupied by the ASPs in the plane was measured. By assuming that each  
375 particle was spherical, we calculated the mean diameter of the ASPs to be 170 nm from  
376 the number and total area of the particles.

377

378 **Acknowledgments**

379 We thank Dr. Alexander A. Chernov, Dr. Saso Štrum and Mr. Sinnosuke Ishizuka for  
380 their suggestions. We also thank Ms. Sakiko Fujita for technical assistance with the  
381 cryo-TEM. This work was supported by the Tohoku University GCOE program for  
382 “Global Education and Research Center for Earth and Planetary Dynamics”, by  
383 Grants-in-Aid from KAKENHI, for Research Activity Start-up (26887001), for Young  
384 Scientists (A) (24684033), and for Scientific Research (S) (15H05731), and by NASA  
385 (Grants NNX14AE79G and NNX14AD68G) and NSF (Grant MCB-1518204). The  
386 cryo-TEM observations were supported by the Nanotechnology Platform Program of  
387 the Ministry of Education, Culture, Sports, Science and Technology (MEXT), Japan.

388

389 **Author contributions:** Y.K. designed the project and experiments. Y.K., T.Y, E.F., M.S.  
390 and H.M. performed the TEM experiments. Y.K. and T.Y. interpreted the data. Y.K., T.Y.,  
391 P.G.V., and A.E.S.V.D. co-wrote the paper. T.Y. performed the optical microscopy  
392 experiments. K.T. supervised the work.

393

394 **Competing interests:** The authors declare that they have no competing interests.

395

396

397

398

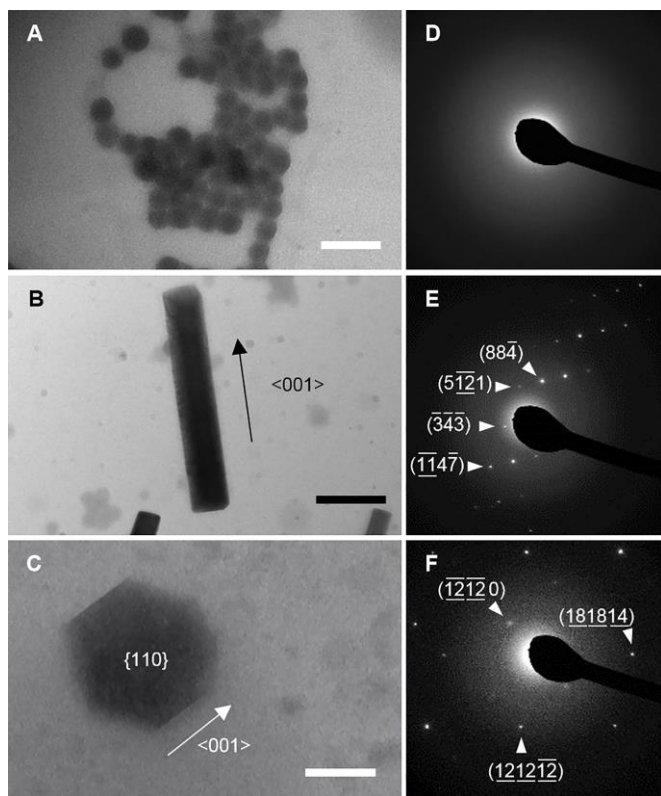
399 **References**

400

- 401 1. Vekilov PG (2012) Crystal nucleation: Nucleus in a droplet. *Nat Mater*  
402 11(10):838–840.
- 403 2. ten Wolde PR, Frenkel D (1997) Enhancement of protein crystal nucleation by  
404 critical density fluctuations. *Science (80- )* 277(5334):1975–1978.
- 405 3. Talanquer V, Oxtoby DW (1998) Crystal nucleation in the presence of a  
406 metastable critical point. *J Chem Phys* 109(1):223–227.
- 407 4. Harano K, et al. (2012) Heterogeneous nucleation of organic crystals mediated by  
408 single-molecule templates. *Nat Mater* 11(10):877–881.
- 409 5. Pouget EM, et al. (2009) The initial stages of template-controlled CaCO<sub>3</sub>  
410 formation revealed by cryo-TEM. *Science (80- )* 323(5920):1455–1458.
- 411 6. Nielsen MH, Aloni S, De Yoreo JJ (2014) In situ TEM imaging of CaCO<sub>3</sub>  
412 nucleation reveals coexistence of direct and indirect pathways. *Science (80- )*  
413 345(6201):1158–1162.
- 414 7. Savage JR, Dinsmore AD (2009) Experimental evidence for two-step nucleation  
415 in colloidal crystallization. *Phys Rev Lett* 102(19):198302.
- 416 8. Muschol M, Rosenberger F (1997) Liquid–liquid phase separation in  
417 supersaturated lysozyme solutions and associated precipitate  
418 formation/crystallization. *J Chem Phys* 107(6):1953–1962.
- 419 9. Sleutel M, Van Driessche AES (2014) Role of clusters in nonclassical nucleation  
420 and growth of protein crystals. *Proc Natl Acad Sci U S A* 111(5):E546-E553.
- 421 10. Maes D, et al. (2015) Do protein crystals nucleate within dense liquid clusters?  
422 *Acta Crystallogr Sect F Struct Biol Commun* 71(7):815–822.
- 423 11. Sauter A, et al. (2015) On the question of two-step nucleation in protein  
424 crystallization. *Faraday Discuss* 179:41–58.
- 425 12. Vorontsova MA, Maes D, Vekilov PG (2015) Recent advances in the  
426 understanding of two-step nucleation of protein crystals. *Faraday Discuss*  
427 179:27–40.
- 428 13. Durek T, Torbeev VY, Kent SBH (2007) Convergent chemical synthesis and  
429 high-resolution x-ray structure of human lysozyme. *Proc Natl Acad Sci*  
430 104(12):4846–4851.
- 431 14. Durbin SD, Feher G (1986) Crystal growth studies of lysozyme as a model for  
432 protein crystallization. *J Cryst Growth* 76(3):583–592.
- 433 15. Nagatoshi Y, et al. (2003) Effects of high pressure on the growth kinetics of

- 434 orthorhombic lysozyme crystals. *J Cryst Growth* 254(1–2):188–195.
- 435 16. Monaco LA, Rosenberger F (1993) Growth and etching kinetics of tetragonal  
436 lysozyme. *J Cryst Growth* 129(3–4):465–484.
- 437 17. Nadarajah A, Forsythe EL, Pusey ML (1995) The averaged face growth rates of  
438 lysozyme crystals: the effect of temperature. *J Cryst Growth* 151(1–2):163–172.
- 439 18. Grogan JM, Schneider NM, Ross FM, Bau HH (2014) Bubble and pattern  
440 formation in liquid induced by an electron beam. *Nano Lett* 14(1):359–364.
- 441 19. Schneider NM, et al. (2014) Electron–water interactions and implications for  
442 liquid cell electron microscopy. *J Phys Chem C* 118(38):22373–22382.
- 443 20. Woehl TJ, Evans JE, Arslan I, Ristenpart WD, Browning ND (2012) Direct in  
444 situ determination of the mechanisms controlling nanoparticle nucleation and  
445 growth. *ACS Nano* 6(10):8599–8610.
- 446 21. Smeets PJM, Cho KR, Kempen RGE, Sommerdijk NAJM, De Yoreo JJ (2015)  
447 Calcium carbonate nucleation driven by ion binding in a biomimetic matrix  
448 revealed by in situ electron microscopy. *Nat Mater* 14(4):394–399.
- 449 22. Chernov AA (1984) *Modern Crystallography III* (Springer Berlin Heidelberg,  
450 Berlin, Heidelberg).
- 451 23. Vekilov PG (2007) What determines the rate of growth of crystals from solution?  
452 *Cryst Growth Des* 7(12):2796–2810.
- 453 24. Vekilov PG, Chernov AA (2003) The physics of protein crystallization. *Solid*  
454 *State Phys* 57:1–147.
- 455 25. Davey RJ, Schroeder SLM, ter Horst JH (2013) Nucleation of organic crystals—a  
456 molecular perspective. *Angew Chemie Int Ed* 52(8):2166–2179.
- 457 26. Trasi NS, Taylor LS (2015) Thermodynamics of highly supersaturated aqueous  
458 solutions of poorly water-soluble drugs—impact of a second drug on the solution  
459 phase behavior and implications for combination products. *J Pharm Sci*  
460 104(8):2583–2593.
- 461 27. Tidhar Y, Weissman H, Tworowski D, Rybtchinski B (2014) Mechanism of  
462 crystalline self-assembly in aqueous medium: a combined cryo-TEM/kinetic  
463 study. *Chem - A Eur J* 20(33):10332–10342.
- 464 28. Thomas BR, Vekilov PG, Rosenberger F (1996) Heterogeneity determination and  
465 purification of commercial hen egg-white lysozyme. *Acta Crystallogr Sect D Biol*  
466 *Crystallogr* 52(4):776–784.
- 467 29. Ewing F, Forsythe E, Pusey M (1994) Orthorhombic lysozyme solubility. *Acta*  
468 *Crystallogr Sect D Biol Crystallogr* 50(4):424–428.
- 469 30. Van Driessche AES, Gavira JA, Patiño Lopez LD, Otalora F (2009) Precise

- 470 protein solubility determination by Laser confocal differential interference  
471 contrast microscopy. *J Cryst Growth* 311(13):3479–3484.
- 472 31. Holtz ME, Yu Y, Gao J, Abruña HD, Muller DA (2013) In situ electron  
473 energy-loss spectroscopy in liquids. *Microsc Microanal* 19(4):1027–1035.
- 474 32. Dold P, Ono E, Tsukamoto K, Sasaki G (2006) Step velocity in tetragonal  
475 lysozyme growth as a function of impurity concentration and mass transport  
476 conditions. *J Cryst Growth* 293(1):102–109.
- 477 33. Oki H, Matsuura Y, Komatsu H, Chernov AA (1999) Refined structure of  
478 orthorhombic lysozyme crystallized at high temperature: correlation between  
479 morphology and intermolecular contacts. *Acta Crystallogr Sect D* 55(1):114–121.
- 480 34. Dubin SB, Clark NA, Benedek GB (1971) Measurement of the rotational  
481 diffusion coefficient of lysozyme by depolarized light scattering: configuration of  
482 lysozyme in solution. *J Chem Phys* 54(12):5158–5164.
- 483 35. Berger MJ, Coursey JS, Zucker MA, Chang J (2005) Data from “Stopping-power  
484 and range tables: electrons, protons, helium ions.” National Institute of Standards  
485 and Technology (NIST). <http://www.nist.gov/pml/data/star/index.cfm/>
- 486 36. James DW (1968) The thermal diffusivity of ice and water between -40 and  
487 +60 °C. *J. Mater. Sci.* 3(5):540–543.
- 488 37. Çengel YA, Boles MA (2006) *Thermodynamics: an engineering approach, 5th ed*  
489 (McGraw-Hill, New York).
- 490  
491  
492



493

494

**Figure 1. The amorphous and crystal phases in supersaturated lysosome solutions.**

495

In situ TEM images of (A) numerous amorphous solid particles (ASPs); (B) an

496

elongated orthorhombic lysozyme crystal; and (C) a tetragonal lysozyme crystal. The

497

corresponding electron-diffraction patterns are shown in (D)–(F), respectively. The

498

arrows in (B) and (C) indicate the  $\langle 001 \rangle$  direction. In (C), the (110) face of the

499

tetragonal lysozyme crystal faces upwards. The scale bars are 500 nm (A), 1  $\mu\text{m}$  (B),

500

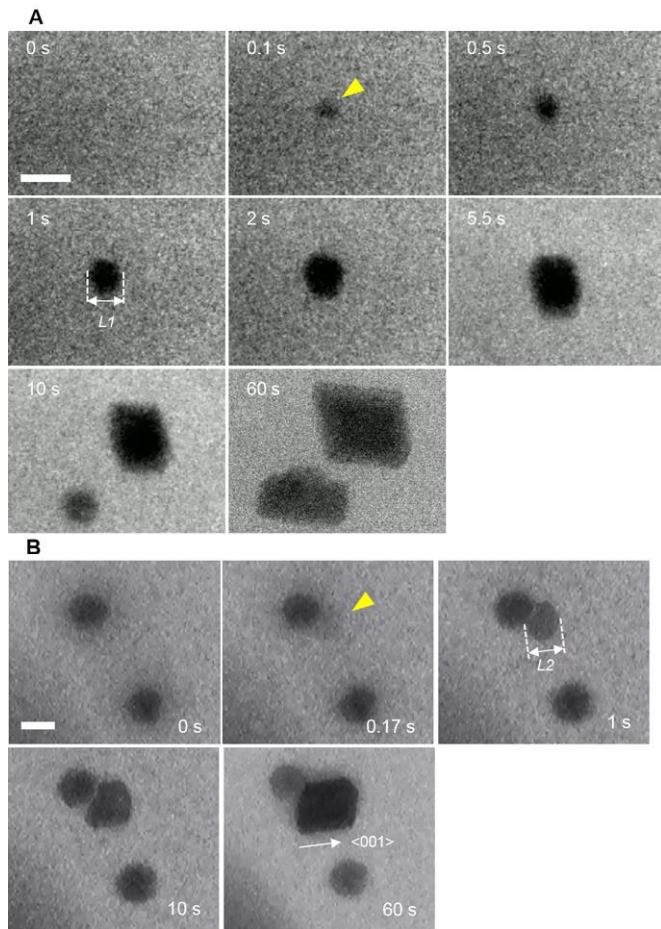
and 200 nm (C). In (E) and (F), the crystal zone axes are  $[\underline{10314}]$  and  $[1 \ -1 \ 0]$ ,

501

respectively.

502

503



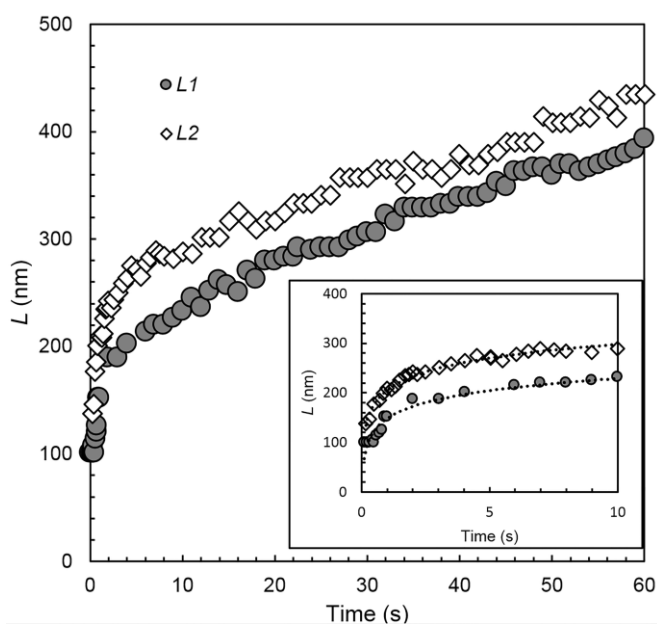
504

505 **Figure 2. The nucleation of lysozyme crystals monitored by time-resolved *in situ***  
 506 **TEM.**

507 (A) A spherical particle observed at 0.1 s (yellow arrowhead) transforms into an  
 508 orthorhombic crystal. A second crystal nucleates at 10 s. The size,  $L1$ , is defined by two  
 509 dashed lines and a bidirectional arrow at 1 s. The scale bar is 200 nm. (B) A spherical  
 510 particle, indicated with a yellow arrowhead, forms at 0.17 s near an amorphous solid  
 511 particle (ASP) and transforms into an orthorhombic crystal. The size,  $L2$ , is defined  
 512 similarly to  $L1$  in (A). The scale bar is 200 nm.

513

514



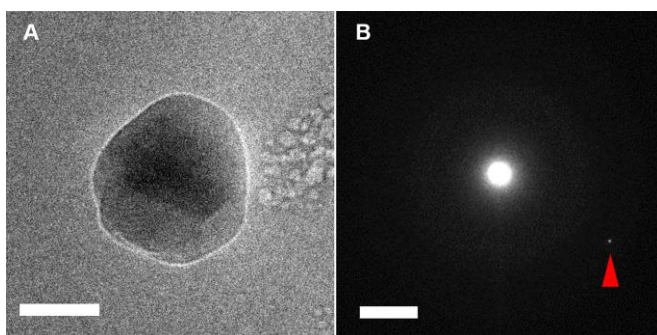
515

516 **Figure 3. The size evolution of nucleated particles.**

517 The size evolutions of particles *L1* in Fig. 2A (circles) and *L2* in Fig. 2B (diamonds)  
 518 reveal decreasing growth rates on average. (Inset) Zoom-in of 0–10 s. Dotted lines are  
 519 logarithmic fits to each data set.

520

521



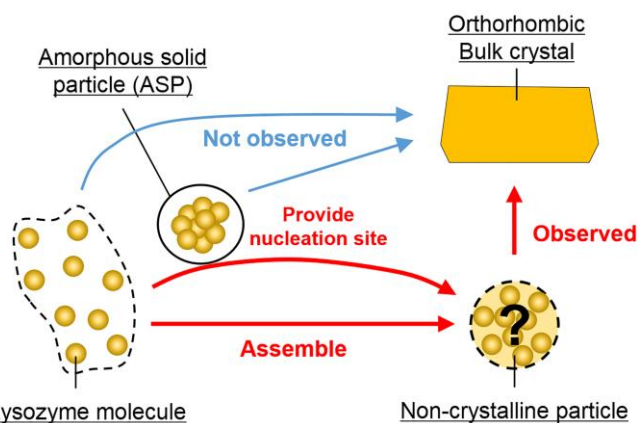
522

523 **Figure 4. Frozen particle with a crystal in its center observed by cryo-TEM.**

524 (A) The particle has a different contrast than the faceted faces, indicating a crystalline  
 525 structure. The scale bar is 50 nm. (B) The corresponding diffraction pattern of the  
 526 particle shows a Laue spot (indicated by a triangle). The scale bar is  $2 \text{ nm}^{-1}$ .

527

528



529

Lysozyme molecule

Non-crystalline particle

530

**Figure 5. Schematic of the nucleation pathway of lysozyme crystals.**

531

Initially, the lysozyme molecules and the ASPs are in the bulk solution. The pathway

532

where molecules assemble into a crystal was not observed. The transformation from the

533

ASP to a crystal was also not observed. Instead, molecules were assembled into

534

non-crystalline particles, for which the detailed features remain undetermined, which

535

heterogeneously nucleate on the container walls or sometimes on the surface of the

536

ASP. Crystal nucleation was observed only via the non-crystalline particles.

537

538 **Supporting Information**

539

540 **SI Text**

541

542 **Calculation of the concentration changes around a growing crystal.**

543 When a crystal of lysozyme is growing in solution, the concentration of lysozyme  
544 molecules in the solution should decrease because of incorporation of molecules into  
545 the crystal surface. To evaluate the effect of this concentration decrement on the growth  
546 rate under TEM, we calculated the concentration of lysozyme molecules around a  
547 growing crystal on the basis of our experimental setup and results.

548 Consider a simple model in which a spherical crystal of radius  $r$  nm is nucleated in a  
549 growth solution in which  $r$  enlarges (grows) isotopically with time. The moment when  
550 nucleation commences ( $r = 0$ ) is defined as  $t = 0$  s, where  $t$  is the time from the  
551 nucleation. Molecules for the growth of the crystal are provided by diffusion from the  
552 growth solution to the crystal, and the volume of the growth solution is defined by  $r$ , the  
553 diffusion length  $l$ , and the thickness of the fluid cell (500 nm). A schematic  
554 representation of this model at time  $t$  is shown in Fig. S8A. We applied this model to the  
555 crystallization of the orthorhombic crystal.

556 The radius  $r(t)$  was calculated using the logarithmic function from fitting in Fig. 3 of *L2*.  
557 The mass of lysozyme in a particle at time  $t$  [ $M_c(t)$ ] can be expressed as follows:

558 
$$M_c(t) = V_c(t)\rho = \frac{4}{3}\pi r^3\rho, \quad (1)$$

559 where  $V_c(t)$  is the volume of the crystal and  $\rho$  is its density. From the structure of the  
560 unit cell of the orthorhombic lysozyme crystal (four molecules in  $5.644 \times 7.373 \times 3.043$   
561 nm (33)), the molecular weight of the lysozyme (14,300), and the Avogadro constant  
562 ( $6.02 \times 10^{23}$ ), the density  $\rho$  is calculated to be  $0.75 \text{ g cm}^{-3}$ . The diffusion length  $l$  can be  
563 expressed as  $l = \sqrt{Dt}$ , where  $D$  is the diffusivity of the lysozyme molecule in the  
564 growth solution, which is  $1.1 \times 10^{-10} \text{ m}^2 \text{ s}^{-1}$  (34).

565 We now consider the mass  $M_s$  of lysozyme molecules that can contribute to crystal  
566 growth in the growth solution. The time at which  $L$  exceeds 500 nm, the thickness of the  
567 liquid cell, is about 0.005 s. Because this time is much smaller than the time resolution  
568 of the TEM movies (recording interval: 157 ms), we can ignore the vertical direction  
569 and assume a cylindrical geometry for the purposes. From the volume of the cylinder  
570 described above and the volume of the nucleated crystal, the volume of the growth  
571 solution  $V_s$  that contains molecules that contribute to crystal growth can be expressed as  
572 follows:

573 
$$V_s(t) = 4\pi(r+l)^2h - \frac{4}{3}\pi r^3 \quad (2)$$

574 The total mass  $M$  of lysozyme molecules in this cylinder is  $V_s C$  (where  $C$  is the initial  
575 concentration of the growth solution  $\sim 15 \text{ mg mL}^{-1}$ ). The value of  $M_s$  can then be  
576 obtained by using  $M$  and  $M_c$ , as follows:

577 
$$M_s(t) = M - M_c = 4\pi(r+l)^2hC - \frac{4}{3}\pi r^3\rho \quad (3)$$

578 Finally, the concentration  $C^*$  in the cylinder at  $t$  is given by the following expression:

579 
$$C^*(t) = \frac{M_s}{V_s} = \frac{3(r+l)^2hC - r^3\rho}{3(r+l)^2h - r^3} \quad (4)$$

580 The description of  $C^*(t)$  is shown in Fig. S8B.

581 According to this calculation,  $C^*(0.15) = 14.992 \text{ mg mL}^{-1}$  is lowest in the range  $0 < t \leq$   
582  $8$ . This decrease in comparison with the initial concentration is only 0.05%. After  $t =$   
583  $0.15$ , the concentration gradually increases because of the decrease in the growth rate.  
584 As a result, the concentration recovers to  $C^*(8) = 14.998 \text{ mg mL}^{-1}$ . The difference in  
585 supersaturation  $\ln(C/C_e) - \ln\{C^*(8)/C_e\}$  is about 0.0005. The expected decrease in the  
586 growth rate of orthorhombic crystals for this difference in supersaturation is about 0.04  
587  $\text{nm s}^{-1}$  in the  $\langle 001 \rangle$  direction under our experimental conditions. Note that this change  
588 in growth rate is too small to explain the decrease in growth rate immediately after the  
589 nucleation under TEM. The change in concentration around the crystal is therefore too  
590 small to affect the growth rate under our experimental conditions.

591

### 592 **Estimation of the temperature elevation of the liquid cell**

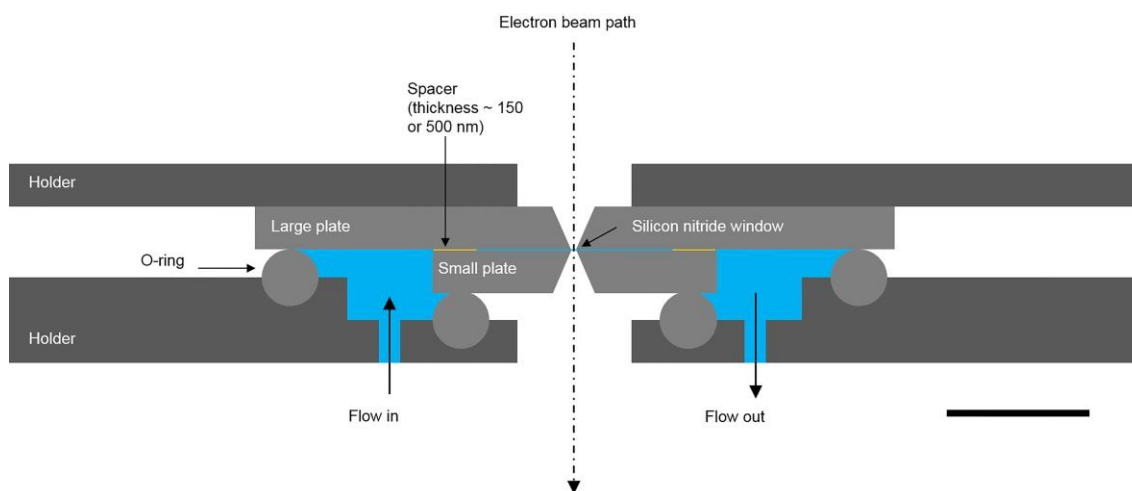
593 To evaluate the temperature elevation by electron beam, we calculated the temperature  
594 in the center of the beam. According to the Grogan *et al.* (18), the maximum  
595 temperature elevation at the center of the beam is

596

597 
$$\Delta T_{max} = \frac{10^2 SI}{\pi\alpha C_p} \left\{ \frac{1}{4} - \frac{1}{2} \ln\left(\frac{L}{a}\right) \right\}, \quad (5)$$

598

599 where  $S$  is the electron stopping power [ $\text{MeV cm}^2 \text{ g}^{-1} \text{ electron}^{-1}$ ],  $I$  is the beam current  
600 [ $\text{C s}^{-1}$ ],  $\alpha$  is the thermal diffusivity of water [ $\text{m}^2 \text{ s}^{-1}$ ],  $C_p$  is the specific heat at constant  
601 pressure of water [ $\text{J g}^{-1} \text{ K}^{-1}$ ],  $L$  is the radius of a disk that has the same area of the  $\text{Si}_3\text{N}_4$   
602 window [ $\text{m}$ ], and  $a$  is the radius of the beam [ $\text{m}$ ]. For calculation, we used  $S = 2.8$  at  
603  $200 \text{ keV}$  (35),  $\alpha = 1.4 \times 10^{-7}$  (36),  $C_p = 4.18$  (37),  $L = 5.6 \times 10^{-5}$ ,  $a = 2.8 \times 10^{-6}$   
604 as typical values, and obtained  $\Delta T_{max} = 1.33$  for our experimental condition.

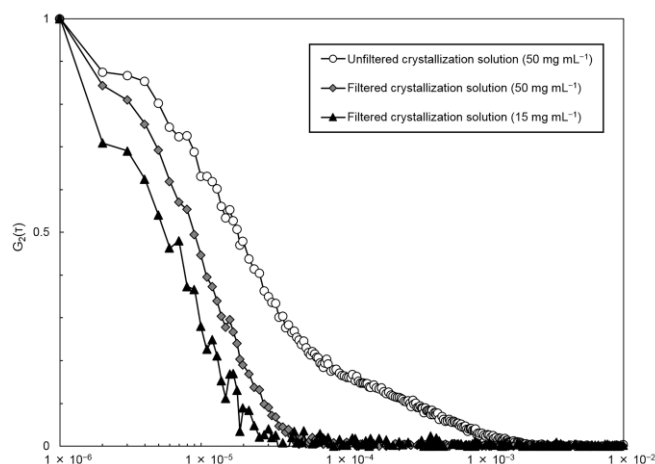


605

606 **Figure S1. Schematic image of the liquid cell for *in situ* TEM observations.**

607 The crystallization solution is located between the small and large plates. Observations  
 608 are performed through the solution layer formed by 150 or 500 nm-thick spacers  
 609 sandwiched between a pair of amorphous silicon nitride windows in the path of the  
 610 electron beam. The size of the available observation area perpendicular to the electron  
 611 beam is  $50 \times 50 \mu\text{m}$ . The growth solution entering the liquid cell flows between the  
 612 large plate and the small plate. The scale bar is 1 mm; the thicknesses of the spacers are  
 613 not to scale.

614

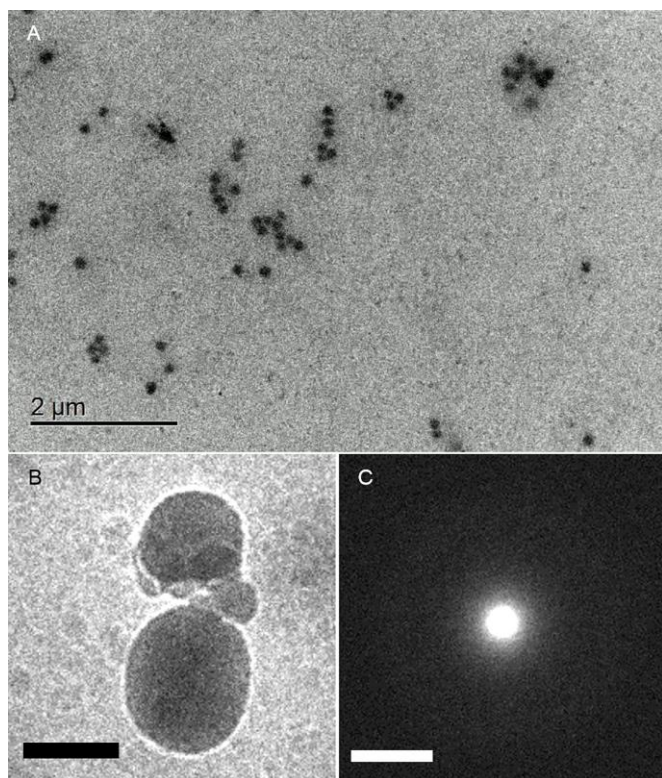


615

616 **Figure S2. Normalized intensity correlation functions of lysozyme solutions.**

617 The three solutions exhibit a decay with characteristic delay time about 20  $\mu\text{s}$ ,  
 618 corresponding to the diffusion time of lysozyme molecules. The unfiltered solution with  
 619 concentration 50  $\text{mg mL}^{-1}$  is the only one that exhibits a second decay with  
 620 characteristic time about 1 ms that suggests the presence of a population of aggregates.

621

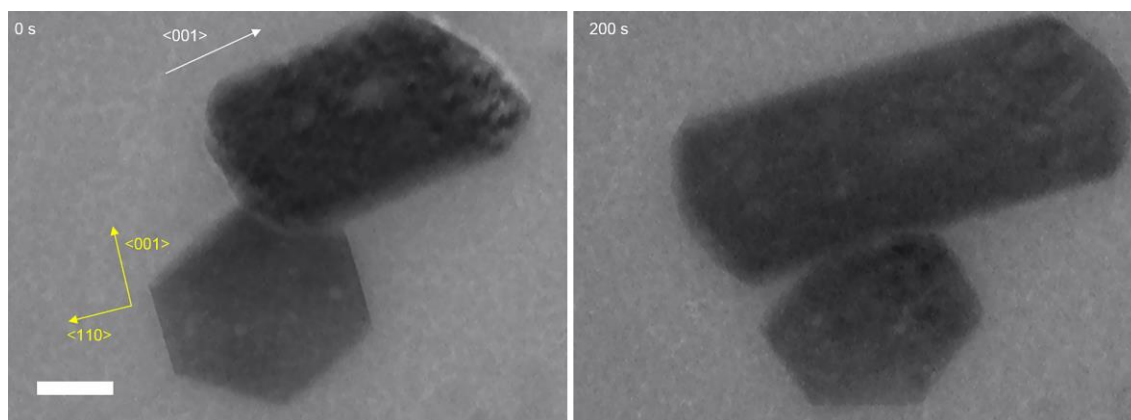


622

623 **Figure S3. Representative TEM images of ASP.**

624 (A) Bright-field *in situ* TEM image of dispersed ASPs in the liquid cell. The mean  
625 diameter of the ASPs in the solution was calculated from the number and total area of  
626 the ASPs, assuming that each ASP is a sphere. (B) Cryo-TEM image of ASPs and (C)  
627 corresponding electron diffraction pattern. The halo pattern shows amorphous structure  
628 of the particles. The scale bars are 200 nm in (B) and 2 nm<sup>-1</sup> in (C), respectively.

629

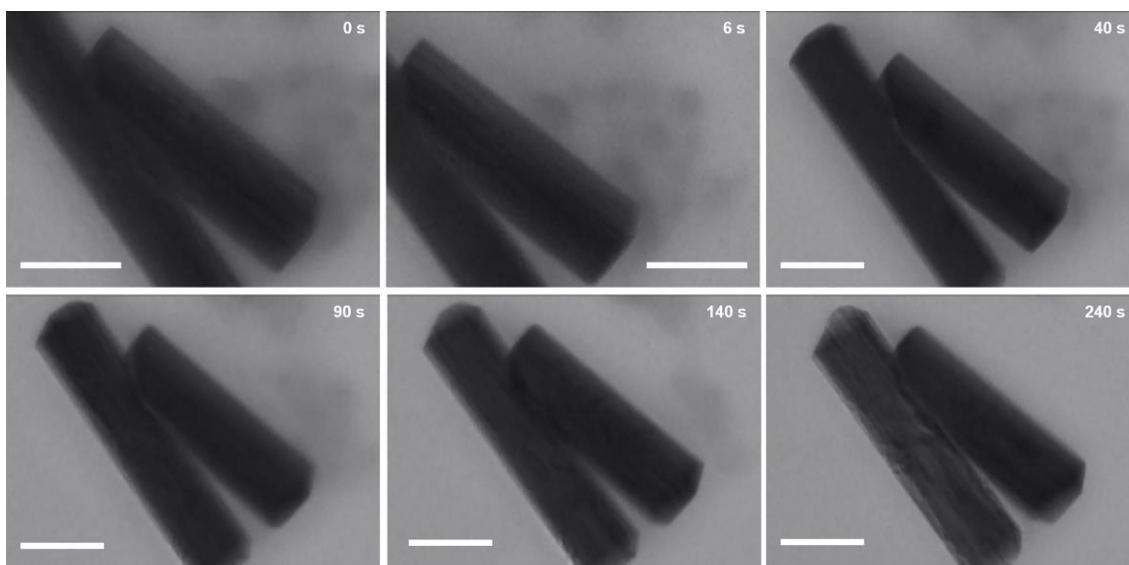


630

631 **Figure S4. The stabilities of the observed crystal phases.**

632 Bright-field *in situ* TEM images show an orthorhombic (upper) and a tetragonal (lower)  
633 lysozyme crystals at 0 and 200 s. The orthorhombic crystal grew by about 400 nm in the  
634 <001> direction (white arrow). In contrast, the tetragonal crystal dissolved by about 70  
635 nm in the <001> direction (yellow arrow), but did not grow or dissolve in the <110>  
636 directions. This image sequence demonstrates that the orthorhombic phase is more  
637 stable than the tetragonal phase under the tested experimental conditions. The scale bar  
638 is 200 nm.

639

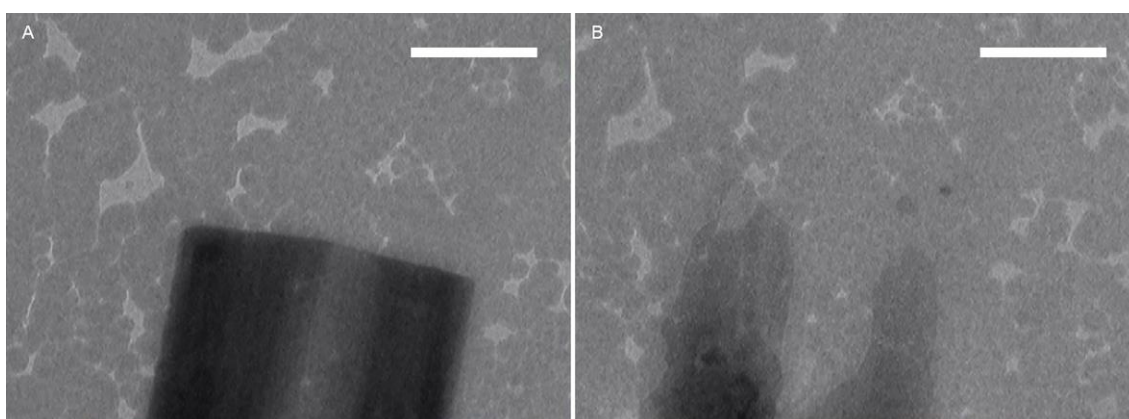


640

641 **Figure S5. The stabilities of the observed phase between orthorhombic crystal and**  
 642 **ASPs.**

643 Bright-field *in situ* TEM images show the two orthorhombic lysozyme crystals and the  
 644 aggregate of ASPs which exists next to crystals. These ASPs gradually dissolved and  
 645 completely disappeared within 240 s. In contrast, the orthorhombic lysozyme crystals  
 646 stably remained. This image sequence demonstrates that the orthorhombic crystal is  
 647 more stable than the ASPs under the tested experimental conditions. The scale bar is  
 648 500 nm.

649

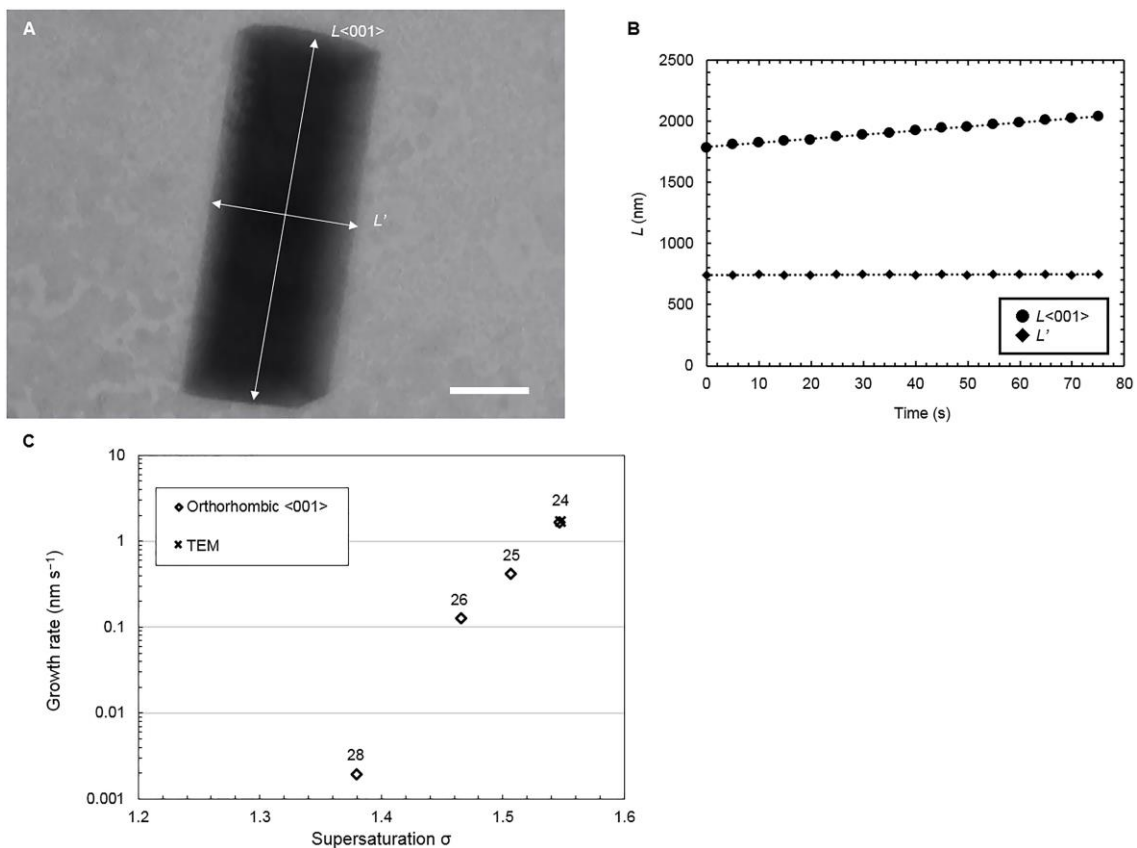


650

651 **Figure S6. The electron beam effects to the orthorhombic lysozyme crystal.**

652 Bright-field *in situ* TEM images show the orthorhombic lysozyme crystal (A) growing  
 653 at  $3.2 \times 10^2$  electron  $\text{nm}^{-2} \text{s}^{-1}$  of the electron flux and (B) dissolved after irradiated  
 654  $2.9 \times 10^3$  electron  $\text{nm}^{-2} \text{s}^{-1}$  of the electron flux. The scale bars are 500 nm.

655

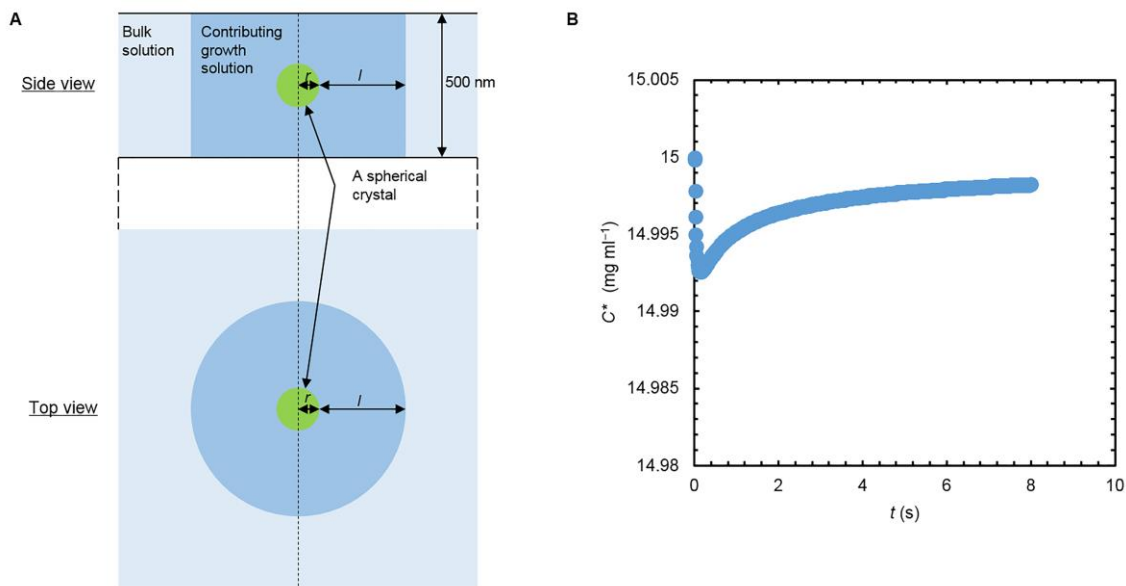


656

657 **Figure S7. Growth rates of the orthorhombic crystals in the presence of electron**  
 658 **irradiation.**

659 (A) Bright-field *in situ* TEM image of an orthorhombic lysozyme crystal. The  
 660 bidirectional arrows labelled  $L_{\langle 001 \rangle}$  and  $L'$  indicate the sizes along the  $\langle 001 \rangle$  direction  
 661 and the direction perpendicular to the  $\langle 001 \rangle$  direction, respectively. The scale bar is 200  
 662 nm. (B) The evolution of  $L_{\langle 001 \rangle}$  and  $L'$  for the crystal shown in (A). The growth rate  
 663 in the  $\langle 001 \rangle$  direction, measured by linear fitting of the appropriate data, was  $1.68 \pm$   
 664  $0.03 \text{ nm s}^{-1}$ . The growth rate in the  $L'$  direction was below the limit of detection. (C)  
 665 Growth rates of orthorhombic lysozyme crystals measured by optical microscopy as a  
 666 function of supersaturation  $\sigma$ . The numbers above the diamonds show the corresponding  
 667 experimental temperature in °C.

668

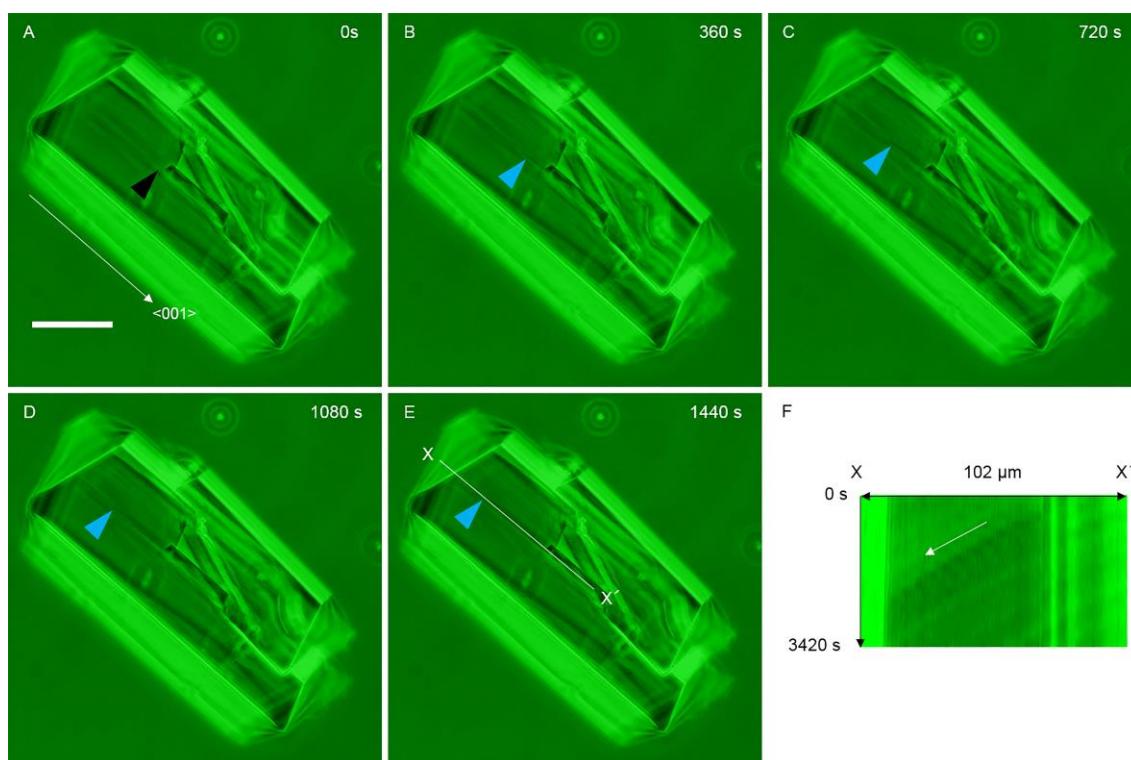


669

670 **Figure S8. Evaluation of concentration variations around a growing particle.**

671 (A) Schematic of the model geometry. A particle of radius  $r$  (shown in green) nucleates  
 672 and grows with the observed growth rate. The volume of the growth solution that  
 673 contributes to the crystal growth is defined by the diffusion length  $l = \sqrt{Dt}$ , where  $D$  is  
 674 the diffusivity of the lysozyme molecule in the growth solution, which is  $1.1 \times 10^{-10} \text{ m}^2$   
 675  $\text{s}^{-1}$  (34). The thickness of the growth cell is 500 nm. (B) The evolution of the lysozyme  
 676 concentration  $C^*$  in contributing growth solution for 8 s after nucleation. The largest  
 677 decrease in  $C^*$  is 0.05% for an initial concentration of  $15 \text{ mg mL}^{-1}$ . This decrement  
 678 should decrease the growth rate by only  $0.04 \text{ nm s}^{-1}$ .

679

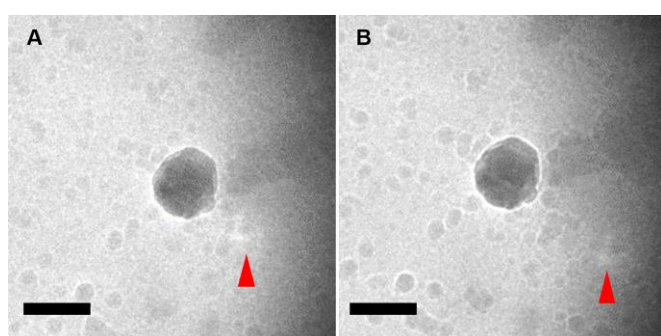


680

681 **Figure S9. Measurement of the step velocity of the orthorhombic lysozyme crystal.**

682 A step on a (110) face of an orthorhombic lysozyme crystal was continuously observed  
 683 at the same position by phase-contrast microscopy (A to E). The black arrowhead in (A)  
 684 indicates the position where the step is generated. The blue arrowheads in (B) to (E)  
 685 indicate the tip of the step. We measured the step velocity in the  $\langle 001 \rangle$  direction from  
 686 the rate of displacement of this tip. A time–space plot image (F) along the X–X' line in  
 687 E shows the movement of the tip of the step along the white arrow in (F). The slope of  
 688 the step trace yields a step velocity of  $44 \text{ nm s}^{-1}$ . The scale bar in (A) is  $50 \mu\text{m}$ .

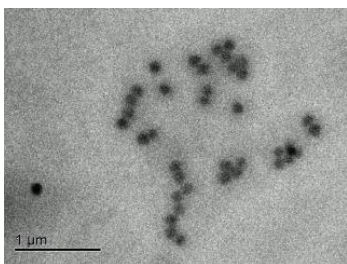
689



690

691 **Figure S10. Freezed particle with a diffraction contrast observed by cryo-TEM.**

692 (A) – (B) The particle under different focus position shows that the diffraction contrasts  
 693 indicated by triangles move with the focus position. This particle is the same as the  
 694 particle in Fig. 4. The scale bars are  $200 \text{ nm}$ .

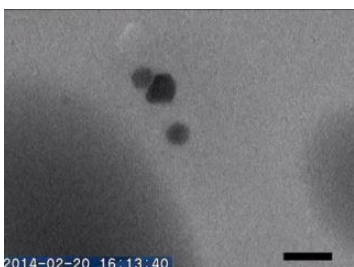


695

696 **Movie S1. The nucleation of an orthorhombic lysozyme crystal within a**  
697 **non-crystalline particle attached to the cell wall monitored by bright-field in situ**  
698 **TEM.**

699 The movie is in real time. Recorded with HF-3300 transmission electron microscope  
700 (Hitachi). The scale bar is 1  $\mu\text{m}$ .

701

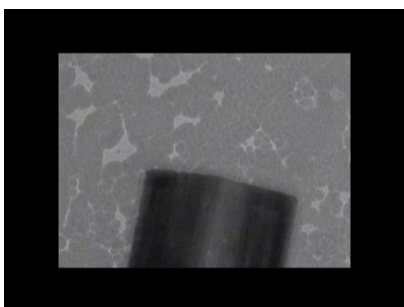


702

703 **Movie S2. The nucleation of an orthorhombic lysozyme crystal within a**  
704 **non-crystalline particle attached to an ASP monitored by bright-field in situ TEM.**

705 The movie is displayed at 2 $\times$  the recording speed; the actual time is displayed in the  
706 lower left-hand corner. Recorder with H-8100 electron microscope (Hitachi). The scale  
707 bar is 500 nm.

708



709

710 **Movie S3. Beam effect to the orthorhombic lysozyme crystal under our**  
711 **experimental conditions.**

712 The movie is displayed at 10 $\times$  speed. Recorder with H-8100 electron microscope  
713 (Hitachi). The actual size of the view field moves from 1.6 $\times$ 2.2  $\mu\text{m}$  to 0.54 $\times$ 0.74  $\mu\text{m}$ ,  
714 then moves back to 1.6 $\times$ 2.2  $\mu\text{m}$ .